Canadian Journal of Pure and Applied Sciences
Vol. 13, No. 3, pp. 4861-4867, October 2019
Online ISSN: 1920-3853; Print ISSN: 1715-9997
Available online at www.cjpas.net

Canadian Journal of pure & applied sciences

# PERFECTLY MATCHED LAYERS SIMULATION IN TWO-DIMENSIONAL VTI MEDIA

*P. Contreras, G. Larrazabal and C. Florio
Multidisciplinary Center for Scientific Visualization and Computation (CEMVICC)
Science Faculty Universidad de Carabobo, Carabobo, Venezuela

## ABSTRACT

Implementing computational boundary conditions such as perfectly matched layers (PML) does have advantages for forwarding modeling of the Earth's crust. The mathematical modeling of many physical problems encountered in industrial applications often leads to a set of linear partial differential equations, PDEs. It considerably improves the visualization of seismic events relevant to oil and gas exploration. In this work, we present an efficient numerical scheme for hyperbolic PDEs, where a computational technique takes care of reflections at the borders domain using a linear two-dimensional (2-D) elastic-wave system of decoupled equations with PML-type boundary conditions. The key idea is to introduce a layer that absorbs the reflections from the borders improving images' visualization. Anisotropy has been reported to occur in the Earth's three main layers: the crust, mantle, and core. However, this implementation refers to the case of a vertical transversal anisotropic medium (VTI) in the crust-layer. Images and screen-shots of the longitudinal (P) impulse-response and the transverse (SV) impulse-response are obtained at deferent times. This computational method enables us to achieve images for the P and SV response-impulses, and to obtain high quality synthetic seismograms for the PP and PS reflection events in a 2-D VTI two-layer model.

**PACS numbers:**07.05.Tp; 94.20.Bb; 91.30.Cd; 91.30.Ab
**Keywords:** Seismic anisotropy, VTI medium, computational modeling, perfectly matched layer.

## INTRODUCTION

The wave equation plays an important role in seismic oil and gas exploration since it allows modeling the earth structure. In the past decades, seismic anisotropy has been gaining attention from academic and industry, in part thanks to advances in anisotropy parameter estimation (Perez *et al*., 1999; Grechka and Tsvankin, 1998).

A material is said to be anisotropic if the value of one or more of its properties varies with direction, consequently anisotropy consideration improves the subsurface imaging. Seismic Anisotropy can be defined as the dependence of seismic velocity on a direction or upon an angle. Anisotropy is described by a $4^{th}$ order elasticity tensor with 21 independent components for the lowest-symmetry case (Musgrave, 1970; Helbig, 1994; Landau and Lifshitz, 1982; Dellinger, 1991). In practice however, observational studies are unable to distinguish all 21 elements and anisotropy considerations are usually simplified. For seismic exploration, the most complicated case occurs in fractured monoclinic media, with 9 elastic constants (Grechka *et al*., 2000). In general, two or more sets of vertical non-corrugated and not perpendicular fractures produce an effective monoclinic medium with a horizontal symmetry plane. The second most important application occurs for the orthorhombic model. The orthorhombic model describes a layered medium fracture in two orthogonal directions (Tsvankin, 1996; Contreras *et al*., 1998). However, in the simplest form (seismic exploration uses it) there are two main kinds of transverse anisotropy, i.e. the transverse isotropy (TI). One is called the horizontal transverse isotropy (HTI), which is a common model in shear-wave studies of fractured reservoirs that describes a system of parallel vertical penny-shaped cracks embedded in an isotropic host rock (Contreras *et al*., 1999). Henceforth this kind of anisotropy is associated with cracks and fractures. The other one is called vertical transversal anisotropy (here VTI means the vertical transversal isotropy) (Thomsen, 1986) and it is associated with layering and shales. Sometimes people call it the vertical polar anisotropy.

In the beginning, forward modeling was done by simulating the scalar *P*-wave field obtained from the acoustic wave equation. However, the earth-crust is elastic and anisotropic (Helbig, 1994; Grechka *et al*., 2000; Contreras *et al*., 1998) and all propagation modes should be considered in order to observe anisotropy effects. Forward modeling and parameter estimation are almost the most fundamental to all other anisotropy applications in oil exploration (Grechka and Tsvankin,

*Corresponding author e-mail: pedrocontre@gmail.com

1998). In part, this can be done by numerically solving the hyperbolic elastic wave equation (WE). The vector and tensor fields representing the WE improve the information about the three-dimensional (3D) earth-crust geology. This translates into a better subsurface imaging and it is of extreme importance for the oil and gas seismic exploration.

The most common type of anisotropy that occurs in the Earth's crust is the VTI that is observed in sedimentary rocks (Winterstein, 1990). To achieve the 3D seismic modeling with the VTI requires the knowledge of five elastic constants. However, in two dimensions only four constants are involved, namely $C_{11}$, $C_{33}$, $C_{13}$, and $C_{44}$. In this work, we use the Voigt notation for the elastic constants (Thomsen, 1986; Faria and Stoffa, 1994). Henceforth shear wave splitting is not considered in a two-dimensional (2-D) modeling because of the lack of the elastic constant $C_{66}$. Abundant geological evidence of shales shows the importance of VTI models in seismic reservoir characterization (Perez *et al.*, 1999; Grechka and Tsvankin, 1998).

In this work, we implement an algorithm using a linear finite difference decoupled PDEs in terms of the velocities and stress tensor components. To implement such a model, we use central-difference second order approximation for space variables and time partial derivatives. Henceforth we use the finite-difference time-domain (FDTD) method (Yee, 1966). In addition, we use staggered stencils for computational storage (Virieux, 1986). Staggered cells grant the calculation of different physical quantities at different mesh-grid points (see Figure 2 in section called **COMPUTATIONAL SPACETIME IMPLEMENTATION**) reducing the computational cost storage. Additionally, with this algorithm we can introduce different source-receiver configurations, making it ideal for simulation in oil and gas seismic modeling.

To implement a FDTD solution of the WE, a computational frame must first be established. The computational domain is the physical region over which the simulation is performed. To achieve the condition of non-reflective borders, we use the artificial technique of perfectly coupled layers PML (Festa and Nielsen, 2003; Komatitsch and Martin, 2007). Consequently, the effect due to the reflection of the waves at the borders of the domain is automatically reduced.

The PML implementation in seismic exploration requires a reformulation of the linear WE to eliminate the unwanted reflections. Thus, this work is structured in the following way. The following section introduces the topic of seismic anisotropy and its relevant application in R&D Oil industry. After that, the next section briefly describes the PDEs for a 2-D medium with VTI shale anisotropy, and the theoretical implementation of the PML obtaining a decoupled EWs (elastic equation system) including the new border computational conditions. Next, the additional section describes the numerical implementation that will allow CPU time reduction. Subsequently, we find the correct decoupled finite-difference scheme in terms of the staggered-stencil mesh taking into consideration the PML (see Fig. 2). In the final section for discussion, the outcome shows the applicability of this technique. We were able to achieve very neat and sharp subsurface images without reflection events at the edges of the 2-D earth-crust two dip layer shale model.

## THE 2-D LINEAR VTI MEDIA

As we stated before, the formulation of a linear WEs in terms of temporal derivatives of the velocity and the stress fields can be used to propagate waves. The FDTD technique reproduces the fields forward in time-domain. This is called forward modeling. This procedure is designed through a 3D staggered finite-difference grid (Faria and Stoffa, 1994). This formulation is widely used in the literature for seismology purposes (Virieux, 1986). In 2-D VTI anisotropy, it involves the transformation of five coupled first-order PDEs, namely the two general equations of motion for the vector velocity ($v_x$, $v_z$) field that are:

$$\rho \frac{\partial v_x}{\partial t} = f_x + \frac{\partial \sigma_{xx}}{\partial x} + \frac{\partial \sigma_{xz}}{\partial z}, \rho \frac{\partial v_z}{\partial t} = f_z + \frac{\partial \sigma_{xz}}{\partial x} + \frac{\partial \sigma_{zz}}{\partial z}$$

where $\rho$ is a constant mass density, $f_x$ and $f_z$ are external forces driven by the source. Since we use the FDTD time-domain technique, a seismic pulse is used as the source, then the response of the system over a wide range of frequencies can be obtained with a single simulation.

And there are the following three equations, where only four elastic constants are used as the input variables for the WEs:

$$\frac{\partial \sigma_{xx}}{\partial t} = C_{11}\frac{\partial v_x}{\partial x} + C_{13}\frac{\partial v_z}{\partial z}$$

$$\frac{\partial \sigma_{zz}}{\partial t} = C_{33}\frac{\partial v_z}{\partial z} + C_{13}\frac{\partial v_x}{\partial x}$$

$$\frac{\partial \sigma_{xz}}{\partial t} = C_{44}\left[\frac{\partial v_x}{\partial z} + \frac{\partial v_z}{\partial x}\right]$$

In three equations written above, the following stress $\sigma_{ij}$ second order tensor field are defined by:

$$\sigma_{ij} = \begin{bmatrix} \sigma_{xx} & \sigma_{xz} \\ \sigma_{zx} & \sigma_{zz} \end{bmatrix}$$

It is noted that the longitudinal (P, i.e. prolongate) and the transverse (SV, i.e. shear-vertical) modes given by the five PDEs written above are coupled (Faria and Stoffa, 1994).

**The2-D decoupled VTI system with PML**

Here we explain ad apply PML technique to the 2-D VTI modeling. In order to make the finite difference method more stable and convergent, we follow the arguments presented previously (Festa and Nielsen, 2003; Komatitsch and Martin, 2007) for the stability and the dispersion conditions in a 2-D EWs. We should mention that a 3D anisotropy implementation has not been completely achieved with this technique due to failures in the stability and dispersion conditions when considering anisotropy (Faria and Stoffa, 1994). However there are some 3D improvements (Festa and Nielsen, 2003). Even in works dedicated to seismology, the use of this technique helps to improve 2-D imaging resolution at larger scales. The seismological domains have borders as it happens in seismic exploration.

The PML mathematical implementation consist in the introduction of a modified coordinate system, where the expansion coefficient is a complex number with an evanescent imaginary part. This generalization is achieved through the following substitution:

$$\frac{\partial}{\partial x} \rightarrow \frac{\frac{\partial}{\partial x}}{1+i\frac{p(x)}{\omega}} \text{ and } \frac{\partial}{\partial z} \rightarrow \frac{\frac{\partial}{\partial z}}{1+i\frac{p(z)}{\omega}}$$

where $p(x)$ and $p(z)$ are the coefficients of the PML. They are given by the following expressions (Komatitsch and Martin, 2007): $p(x) = p_0\,(x/L)^N$ and $p(z) = p_0\,(z/L)^N$ with $p_0 = -3v_p\,\log(R_c)/(2L)$, where $L$ is the thickness of the perfectly coupled layer, $N$ the size of the problem, and $p_0$ has an approximate value of 341.9.

When the above coordinate system is replaced in the equations for the VTI medium of the previous section, the system becomes a new linear decoupled PDE-EWs. Because of the applied replacement there appear the following new equations for the new decoupled velocities $v_x^1$ and $v_x^2$:

$$\rho\left[\frac{\partial}{\partial t}+p(x)\right]v_x^1 = f_x + \frac{\partial \sigma_{xx}}{\partial x}, \rho\left[\frac{\partial}{\partial t}+p(z)\right]v_x^2 = \frac{\partial \sigma_{xz}}{\partial z}$$

For the decoupled velocities $v_z^1$ and $v_z^2$, the equations are:

$$\rho\left[\frac{\partial}{\partial t}+p(x)\right]v_z^1 = f_z + \frac{\partial \sigma_{xz}}{\partial x}, \rho\left[\frac{\partial}{\partial t}+p(z)\right]v_z^2 = \frac{\partial \sigma_{zz}}{\partial z}$$

These decoupled velocities (Komatitsch and Martin, 2007) are related to the coupled ones by the relation $v_x = v_x^1 + v_x^2$ and $v_z = v_z^1 + v_z^2$.

The stress tensor field is mathematically treated in the same way, obtaining a decoupled set of the new stress equations. The new decoupled stress ($\sigma_{xx}^1$ and $\sigma_{xx}^2$) equations are:

$$\left[\frac{\partial}{\partial t}+p(x)\right]\sigma_{xx}^1 = C_{11}\frac{\partial v_x}{\partial x}, \left[\frac{\partial}{\partial t}+p(z)\right]\sigma_{xx}^2 = C_{13}\frac{\partial v_z}{\partial z}$$

Also, the new equations for the decoupled stress tensors components $\sigma_{zz}^1$ and $\sigma_{zz}^2$ are equal to:

$$\left[\frac{\partial}{\partial t}+p(x)\right]\sigma_{zz}^1 = C_{13}\frac{\partial v_x}{\partial x}, \left[\frac{\partial}{\partial t}+p(z)\right]\sigma_{zz}^2 = C_{33}\frac{\partial v_z}{\partial z}$$

The decoupled shear stress tensor components $\sigma_{xz}^1$ and $\sigma_{xz}^2$ follow the equations:

$$\left[\frac{\partial}{\partial t}+p(x)\right]\sigma_{xz}^1 = C_{44}\frac{\partial v_z}{\partial x}, \left[\frac{\partial}{\partial t}+p(z)\right]\sigma_{xz}^2 = C_{44}\frac{\partial v_x}{\partial z}$$

where now $\sigma_{xx} = \sigma_{xx}^1 + \sigma_{xx}^2$, $\sigma_{zz} = \sigma_{zz}^1 + \sigma_{zz}^2$, and $\sigma_{xz} = \sigma_{xz}^1 + \sigma_{xz}^2$. These five linear PDE equations will be used for a forward modeling in the following section.

**THE COMPUTATIONAL SPACETIME IMPLEMENTATION**

The computational model that we propose in this simulation is divided into a mesh of $N_x \times N_z$ points. The finite-difference scheme shown in Figure 1 demonstrates the computational edge domain where the PML are applied according to the two-layer dip model. $\Delta x$ and $\Delta z$ are defined as the distances between the points in such a way that $x = n_x\Delta_x$ and $z = n_z\Delta z$ with $n_x = 1...N_x$ and $n_z = 1...N_z$. For the timestep $\Delta t$, we have $t = n\Delta t$, where $n$ the timestep shown in Figure 2, and the stencil time is not showed (Faria and Stoffa, 1994).

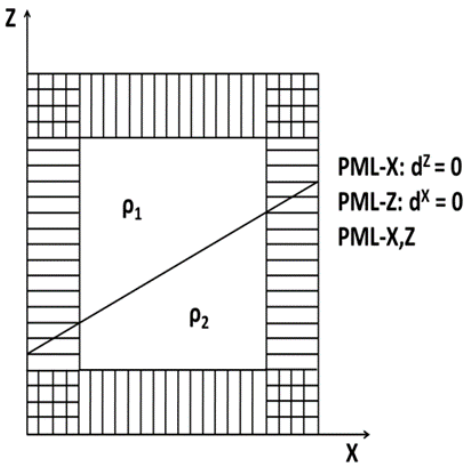


Fig. 1. The finite-difference simplified scheme showing the computational two-layer dip model. The vertical, horizontal, and crossed lines near the borders show the spots where the PLM are applied.

The five variables $v_x^1$, $v_z^1$, $\sigma_{xx}^1$, $\sigma_{zz}^1$, and $\sigma_{xz}^1$ are discretized into a 2-D staggered grid mesh, see in Figure 2 for a better explanation, where the velocity components are stored in both stencils, the normal components of the stress tensors are stored in one of the stencils, while the shear stress components are located at another stencil. However, the major difference of a staggered-grid scheme is that the velocity and stress components are not known at the same grid point, as it can be seen in Figure 2. Henceforth we use a previous scheme proposal with little modifications (Faria and Stoffa, 1994), where different stencils are used for normal and shear stress field computations.

Following scheme shown in Figure 2, domain $v_x$ is calculated at the points ($i$ ± 1/2, $k$) in the space, $v_z$ is calculated at the points ($i$, $k$ ± 1/2), the normal stress tensor components $\sigma_{xx}$ and $\sigma_{zz}$ are calculated at the points ($i$, $k$) and finally the shear stress $\sigma_{xz}$ is calculated at the points ($i$ ± 1/2, $k$ ± 1/2). The density $\rho(x, y, z)$ is considered a constant density $\rho_0$, see the last line of table 1 for its correspondent values and units. Physically it means that the VTI model is homogeneous and that does not take into consideration earth-crust heterogeneities.

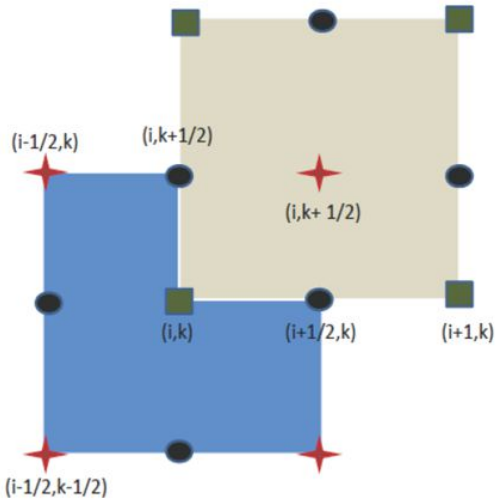


Fig. 2. The staggered finite-difference grid for the velocity and stress updates; both stencils show the grids points, where different fields components are calculated. The velocity components are calculated in both stencils (black circles), the shear stress components are calculated in the blue stencil (red stars), and the cinnamon stencil is used to calculate the normal stress components (green squares).

An explosive source is simulated using the amplitude of a Ricker wavelet with a peak frequency $f_0$~ 30 Hertz. Amplitudes are added to the velocities $v_x^1$ and $v_z^1$ at each $n$ timestep. The stability limit of the discrete system is given by the following condition:

$$\Delta t < 0.606\Delta x/V_p$$

where $V_p$ stands for the horizontal longitudinal speed (Faria and Stoffa, 1994).

The dispersion condition for the discrete system is given by the inequality:

$$\Delta x < V_s/(10f_0)$$

where $V_s$ is the transverse wave speed.

However, some authors (Becache *et al.*, 2003) showed that the stability of the classical PML model depends upon the physical properties of the anisotropic medium and that it can be intrinsically unstable. However, the elastic constants listed in the table were previously proven (Faria and Stoffa, 1994) to meet the Becache stability criteria. This algorithm could be extended to 3D situations by further studying the stability and dispersion conditions.

Henceforward we proceed to obtain the discretization of the velocity fields as follows. For the decoupled finite-difference system, the $v_x^1$ and $v_x^2$ components are computed at time-step points $t^{n+1}$ and $t^n$(the stencil-time is not shown in (Faria and Stoffa, 1994)) with the following finite-difference equations:

$$v_x^1|_{i+1/2,k}^{n+1} = v_x^1|_{i+1/2,k}^{n} e^{-p(x)\Delta t} + \frac{1}{\rho}\frac{\Delta t}{\Delta x} e^{-0.5p(x)\Delta t}\left[\sigma_{xx}|_{i+1,k}^{n+1/2} - \sigma_{xx}|_{i,k}^{n+1/2}\right] \quad (1)$$

$$v_x^2|_{i+1/2,k}^{n+1} = v_x^1|_{i+1/2,k}^{n} e^{-p(z)\Delta t} + \frac{1}{\rho}\frac{\Delta t}{\Delta z} e^{-0.5p(z)\Delta t}\left[\sigma_{xz}|_{i+1/2,k+1/2}^{n+1/2} - \sigma_{xz}|_{i+1/2,k-1/2}^{n+1/2}\right] \quad (2)$$

The $v_z^1$ and $v_z^2$ components are calculated at the time-step points $t^{n+1}$ and $t^n$ with the help of the following equations:

$$v_z^1|_{i,k+1/2}^{n+1} = v_z^1|_{i,k+1/2}^{n} e^{-p(x)\Delta t} + \frac{1}{\rho}\frac{\Delta t}{\Delta x} e^{-0.5p(x)\Delta t}\left[\sigma_{xz}|_{i+1/2,k+1/2}^{n+1/2} - \sigma_{xz}|_{i-1/2,k+1/2}^{n+1/2}\right] \quad (3)$$

$$v_z^2|_{i,k+1/2}^{n+1} = v_z^1|_{i,k+1/2}^{n} e^{-p(z)\Delta t} + \frac{1}{\rho}\frac{\Delta t}{\Delta z} e^{-0.5p(z)\Delta t}\left[\sigma_{xx}|_{i,k+1}^{n+1/2} - \sigma_{xx}|_{i,k}^{n+1/2}\right] \quad (4)$$

For the stress fields, the discretization is as follows. First, the decoupled equations for the normal stress tensor components $\sigma_{xx}^1$ and $\sigma_{xx}^2$ are computed at the mesh step-time points $t^{n\pm1/2}$ using the equations:

$$\sigma_{xx}^{1}|_{i,k}^{n+1/2} = \sigma_{xx}^{1}|_{i,k}^{n-1/2} e^{-p(x)\Delta t} + C_{11}\frac{\Delta t}{\Delta x} e^{-0.5p(x)\Delta t}\left[v_x|_{i+1/2,k}^{n} - v_x|_{i-1/2,k}^{n}\right] \quad (5)$$

$$\sigma_{xx}^{2}|_{i,k}^{n+1/2} = \sigma_{xx}^{2}|_{i,k}^{n-1/2} e^{-p(z)\Delta t} + C_{13}\frac{\Delta t}{\Delta z} e^{-0.5p(z)\Delta t}\left[v_z|_{i,k+1/2}^{n} - v_z|_{i,k-1/2}^{n}\right] \quad (6)$$

Second, the decoupled equation for the normal stress components $\sigma_{zz}^{1}$ and $\sigma_{zz}^{2}$ are computed at the time points $t^{n\pm1/2}$ by means of the following expressions:

$$\sigma_{zz}^{1}|_{i,k}^{n+1/2} = \sigma_{zz}^{1}|_{i,k}^{n-1/2} e^{-p(x)\Delta t} + C_{13}\frac{\Delta t}{\Delta x} e^{-0.5p(x)\Delta t}\left[v_x|_{i+1/2,k}^{n} - v_x|_{i-1/2,k}^{n}\right] \quad (7)$$

$$\sigma_{zz}^{2}|_{i,k}^{n+1/2} = \sigma_{zz}^{2}|_{i,k}^{n-1/2} e^{-p(z)\Delta t} + C_{33}\frac{\Delta t}{\Delta z} e^{-0.5p(z)\Delta t}\left[v_z|_{i,k+1/2}^{n} - v_z|_{i,k-1/2}^{n}\right] \quad (8)$$

Third, the decoupled equations for the shear components $\sigma_{xz}^{1}$ and $\sigma_{xz}^{2}$ are computed at time points $t^{n\pm1/2}$ by means of:

$$\sigma_{xz}^{1}|_{i+1/2,k+1/2}^{n+1/2} = \sigma_{zz}^{1}|_{i+1/2,k+1/2}^{n-1/2} e^{-p(x)\Delta t} + C_{44}\frac{\Delta t}{\Delta x} e^{-0.5p(x)\Delta t}\left[v_z|_{i+1/2,k}^{n} - v_z|_{i-1/2,k}^{n}\right] \quad (9)$$

$$\sigma_{xz}^{2}|_{i+1/2,k+1/2}^{n+1/2} = \sigma_{zz}^{1}|_{i+1/2,k+1/2}^{n-1/2} e^{-p(z)\Delta t} + C_{44}\frac{\Delta t}{\Delta z} e^{-0.5p(z)\Delta t}\left[v_x|_{i,k+1/2}^{n} - v_x|_{i,k+1/2}^{n}\right] \quad (10)$$

The elastic constants used for the two-layer model are given according to the table. These values correspond to different types of VTI media and they are able to accomplish the stability condition using a PML computer domain (Faria and Stoffa, 1994; Komatitsch and Martin, 2007; Becache *et al*., 2003).

Table 1. The VTI elastic constants for the model shown in Figure 4a (Komatitsch and Martin, 2007).

| Elastic constants, $10^{10}$ [N/m$^2$] | upper layer | bottom layer |
|---|---|---|
| $C_{11}$ | 16.5 | 16.7 |
| $C_{13}$ | 5.0 | 6.6 |
| $C_{33}$ | 6.2 | 14.0 |
| $C_{44}$ | 3.4 | 6.63 |
| $\rho_0$ [kg/m$^3$] | 7,100 | 3,200 |

## DISCUSSION

The present paper describes a new spacetime 2-D methodology with timestep and spacestep control to solve 2-D VTI linear decoupled EWs with PML conditions using staggered-grids shown in Figures 1 and 2. Henceforth, we develop a computational model for an elastic wave propagation simulation for 2-D VTI anisotropic media, by combining a FDTD method on staggered grids with a PML boundary condition. For that, a High-Performance Linux application in C (over 1,000 lines of code) using Make, GDB and Valgrinds memcheck, to generate and visualize 2-D response-impulses and synthetic seismograms were developed.

We establish that visualization of the impulse response of the P and SV modes can be improved by the PML. As a consequence, unwanted reflections from the borders shown in Figure 3 are totally eliminated according to Virieux (1986).

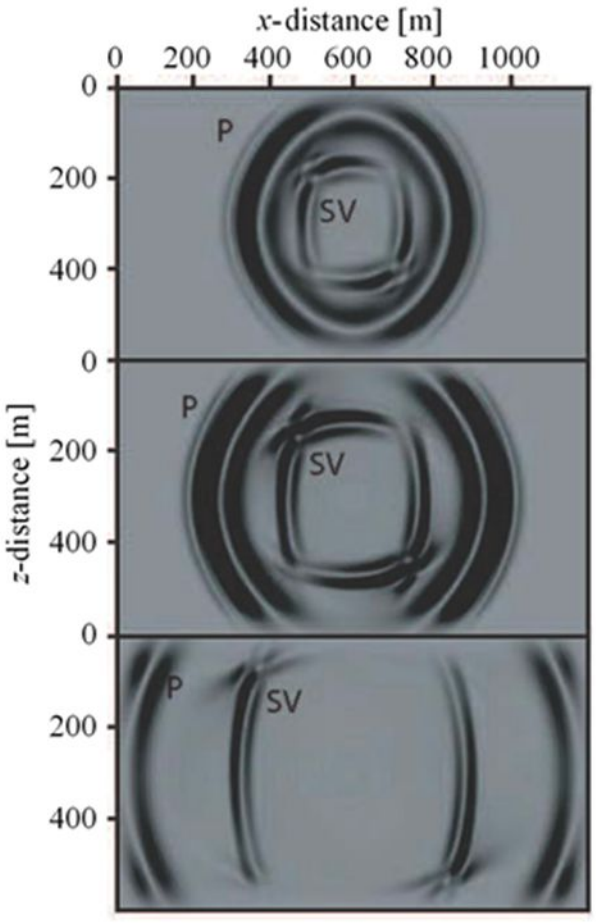


Fig. 3. The screenshots at 0.2 (the upper), 0.3, and 0.5 second are displayed for the vertical velocity wave-field component propagating through a homogeneous medium with elastic constants from the upper layer listed in the Table 1. The triplication of the SV wave around the intermediate angles are observed to be asymmetrical for

the SV impulse-response. The absorbing effect of the PML at the edges of the computational domain is notable.

Figure 3, while the SV response-impulse presents triplications. Moreover, the effects of the VTI elastic constants on SV response-impulses affects the direction of propagation. We observe from the snapshots in Figure 3

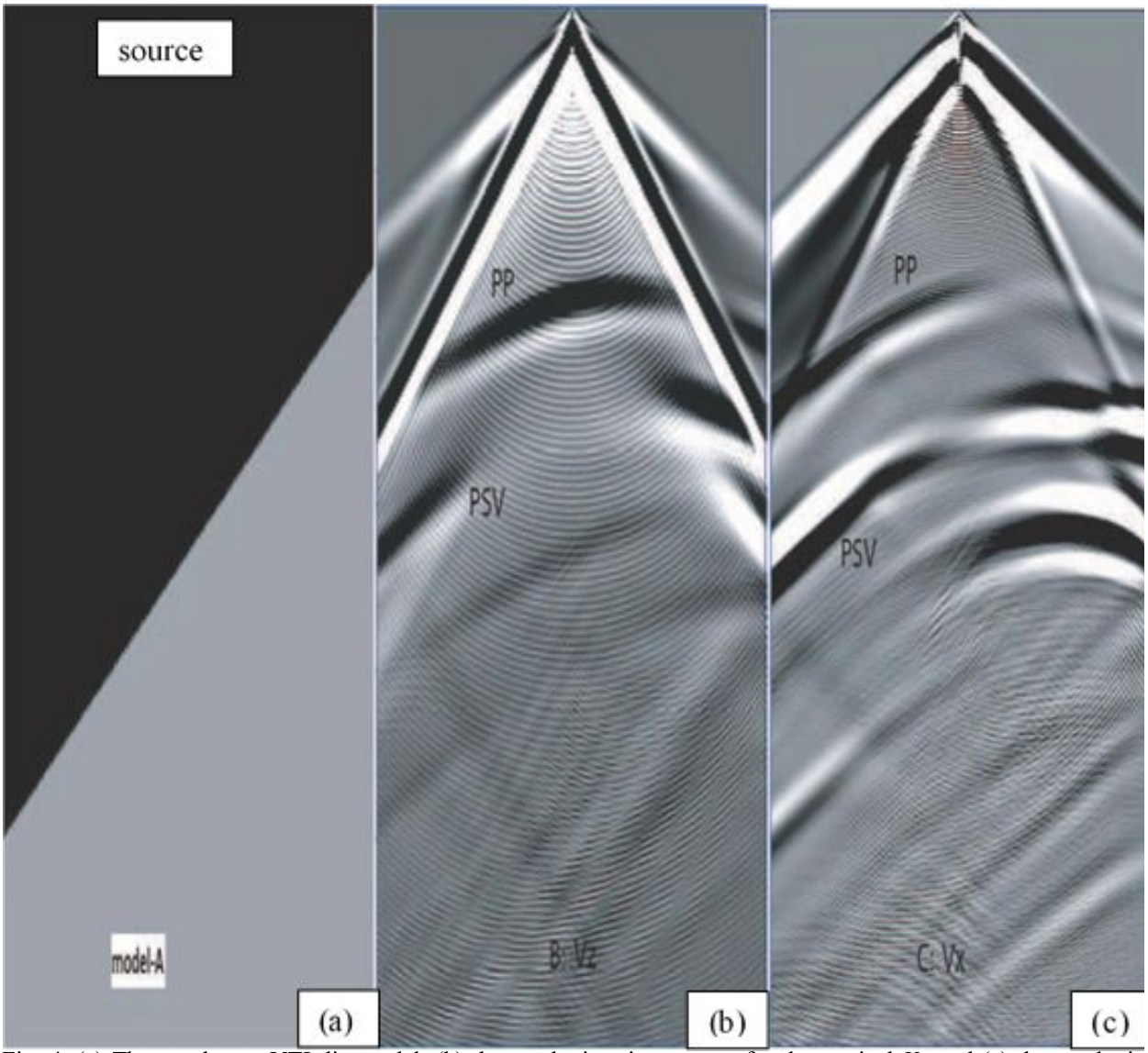


Fig. 4. (a) The two-layers VTI dip model; (b) the synthetic seismograms for the vertical $V_z$; and (c) the synthetic seismograms for the horizontal $V_x$. Both the PP and PSV reflection events due to the dip layer are presented in screenshots (b) and (c).

In Figure 3, the simulations were performed with an explosive source (Ricket-wavelength) centered in the middle of the model to eliminate reflections from the edges. In Figure 3, time screenshots for t = 0.2, 0.3, and 0.5 second are also presented. From those snapshots, we conclude that the PML boundary conditions absorb the reflections from the border, implying an exceptional numerical performance of the computational PML technique. Another conclusion is that the P 2-D response-impulse behave as a simpler quasi-elliptical way shown in

how the value of the elastic constant $C_{13}$ affects the direction of the SV. Triplications in the SV wavefront are modeled. However, one question is not solved yet in this work: the asymmetric behavior of the SV impulse-response in Figure 3 with respect to the vertical axis.

Subsequently, the explosive source is relocated to the upper central part of the 2-D model sketched in Figure 4a. On the surface, fifty receivers are uniformly distributed on both sides of the source. We see how the velocity fields

cancel out at the edges of the model in Figure 4a. Then we obtain the synthetic seismograms for the two layers model, each of them has different elastic constants values. The synthetic seismograms of the vertical component $V_z$ (Fig. 4b) and the horizontal component $V_x$ (Fig. 4c) are shown with the primary reflections events due to the dip layer. In addition, Figure 5 shows the elastic P response-impulse propagating from the middle of the top through the model shown in Figure 4a.

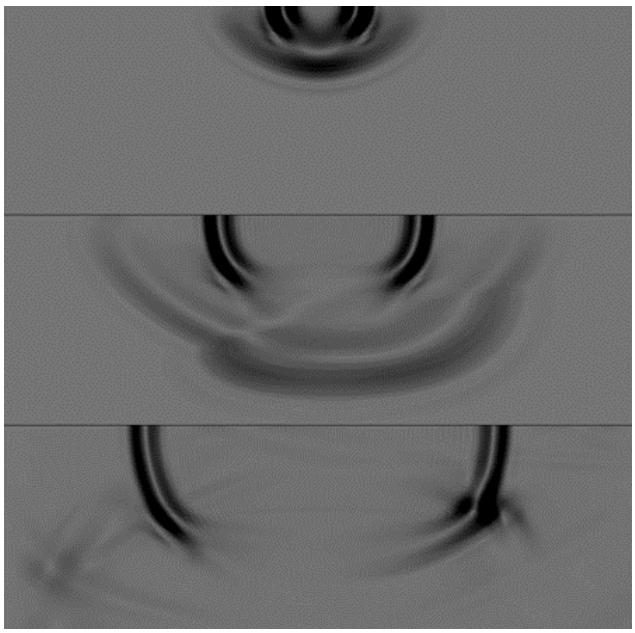

Fig. 5. The elastic P response-impulse propagating from the middle of the top through the model shown in Figure 4a.

## CONCLUSION

This short report remarkably showed the effectiveness of the PML using the decoupled linear system of equations (1)-(10) for the 2-D VTI media simulation in Oil and Gas R&D.

## ACKNOWLEDGMENT

One of the authors, P. Contreras wishes to express his gratitude to Dr. V. Grechka from Marathon Oil for pointing out an invariant symmetric question for the SV impulse-response. The authors also acknowledge Drs. E. Sanchez from ASML, and Prof. J. Moreno from UDE for several discussions regarding the numerical implementation of this work.

## REFERENCES

Becache, E., Fauqueux, S. and Joly, P. 2003. Stability of perfectly matched layers, group velocities and anisotropic waves. Journal of Computational Physics. 188(2):399-433.

Contreras, P., Klie, H. and Michelena, R. 1998. In: The 68th Annual International Meeting of the Society of Exploration Geophysists. pp1491.

Contreras, P., Grechka, V. and Tsvankin, I. 1999. Moveout inversion of P-wave data for horizontal transverse isotropy. Geophysics. 64(4):1219-1229.

Dellinger, J. 1991. Anisotropic seismic wave propagation. Ph.D. thesis. Stanford University.

Faria, EL. and Stoffa, PL. 1994. Finite-difference modeling in transversely isotropic media. Geophysics. 59(2):282-289.

Festa, G. and Nielsen, S. 2003. PML absorbing boundaries. Bulletin of the Seismological Society of America. 93(2):891-903.

Grechka, V. and Tsvankin, I. 1998. 3-D description of normal moveout in anisotropic inhomogeneous media. Geophysics. 63(3):1079-1092.

Grechka, V., Contreras, P. and Tsvankin, I. 2000. Inversion of normal moveout for monoclinic media. Geophysical Prospecting. 48:577-602.

Helbig, K. 1994. Foundations of anisotropy for exploration seismics. In: Handbook of Geophysical Exploration, Seismic Exploration (vol. 22). Elsevier Science/Pergamon Press.

Komatitsch, D. and Martin, R. 2007. An unsplit convolutional Perfectly Matched Layer improved at grazing incidence for the seismic wave equation. Geophysics. 72(5):SM155-SM167.

Landau, LD. and Lifshitz, EM. 1982. Elasticity Theory. Pergamon Press, UK.

Musgrave, MJP. 1970. Crystal Acoustics. Holden-Day, San Francisco. pp288.

Perez, MA., Grechka, V. and Michelena, RJ. 1999. Fracture detection in a carbonate reservoir using a variety of seismic methods. Geophysics. 64(4):1266-1276.

Thomsen, L. 1986. Weak elastic anisotropy. Geophysics. 51(10):1954-1966.

Tsvankin, I. 1996. Effective parameters and p-wave velocity for orthorhombic anisotropy. In: The 66th Annual International Meeting of the Society of Exploration Geophysists. pp1850.

Virieux, J. 1986. P-SV wave propagation in heterogeneous media, velocity-stress finite difference method. Geophysics. 51(4):889-901.

Winterstein, DF. 1990. Velocity anisotropy terminology for geophysicists. Geophysics. 55(8):1070-1088.

Yee, KS. 1966. Numerical solution of initial boundary value problems involving Maxwell's equations in isotropic media. The IEEE Transactions on Antennas and Propagation. 14(3):302-307.

Revised: July 5, 2019; Accepted: Sept 26, 2019